Title
Colloidal Synthesis Path to 2D Crystalline Quantum Dot Superlattices

Journal
ACS Nano, 15(2)

ISSN
1936-0851

Authors
Ondry, Justin C
Philbin, John P
Lostica, Michael
et al.

Publication Date
2021-02-23

DOI
10.1021/acsnano.0c07202

Peer reviewed

Colloidal Synthesis Path to 2D Crystalline Quantum Dot Superlattices

Justin C. Ondry,[†,‡] John P. Philbin,[†,⊥] Michael Lostica,[†] Eran Rabani,[†,¶,§] and A. Paul Alivisatos[*,†,‡,¶,‖]

†*Department of Chemistry, University of California, Berkeley, California 94720, United States*

‡*Kavli Energy NanoScience Institute, Berkeley, California 94720, United States*

¶*Materials Sciences Division, Lawrence Berkeley National Laboratory, Berkeley, California 94720, United States*

§*The Sackler Center for Computational Molecular and Materials Science, Tel Aviv University, Tel Aviv, Israel 69978*

‖*Department of Materials Science and Engineering, University of California, Berkeley, California 94720, United States*

⊥*Current address: John A. Paulson School of Engineering and Applied Sciences, Harvard University, Cambridge, Massachusetts 02138, United States*

E-mail: paul.alivisatos@berkeley.edu

Abstract

By combining colloidal nanocrystal synthesis, self assembly, and solution phase epitaxial growth techniques, we developed a general method for preparing single dot thick atomically attached quantum dot (QD) superlattices with high quality translational and crystallographic orientational order along with state-of-the-art uniformity

in the attachment thickness. The procedure begins with colloidal synthesis of hexagonal prism shaped core/shell QDs (*e.g.* CdSe/CdS), followed by liquid subphase self-assembly and immobilization of superlattices on a substrate. Solution phase epitaxial growth of additional semiconductor material fills in the voids between the particles resulting in a QD-in-matrix structure. The photoluminescence emission spectra of the QD-in-matrix structure retains characteristic 0D electronic confinement. Importantly, annealing of the resulting structures removes inhomogeneities in the QD-QD inorganic bridges, which our atomistic electronic structure calculations demonstrate would otherwise lead to Anderson-type localization. The piece-wise nature of this procedure allows one to independently tune the size and material of the QD core, shell, QD-QD distance, and the matrix material. These four choices can be tuned to control many properties (*e.g.* degree of quantum confinement, quantum coupling, band alignments, *etc.*) depending on the specific applications. Finally, cation exchange reactions can be performed on the final QD-in-matrix, as demonstrated herein with a CdSe/CdS to HgSe/HgS conversion.

Keywords

self assembly, oriented attachment, nanocrystal superlattices, quantum dots, CdSe

Introduction

Colloidal semiconductor nanocrystals are often called "artificial atoms" because they display tuneable hydrogen-like wavefunctions.[1,2] Colloidal nanocrystals are known to readily assemble into crystalline superlattices[3,4] converting the "artificial atoms" into an "artificial solid". As such, one would expect linear combinations of the "superatomic" orbitals to give rise to a mini-band structure. The structural diversity of nanocrystal superlattices and the continuous tunability of nanocrystal electronic states suggests substantial potential for band structure engineering. Unfortunately, in most cases, semiconductor nanocrystal superlattices

do not display the sought after mini-band electronic structure.

We qualitatively consider the parameters needed to realize delocalized states in a quantum dot superlattice with a tight binding Hamiltonian,[5]

$$H = \sum_i \varepsilon_i a_i^\dagger a_i + \sum_{\langle ij \rangle} t_{ij}(a_i^\dagger a_j + h.c.) \tag{1}$$

where ε_i is the on-site energy, t_{ij} is the coupling between sites that is only non-zero for site pairs ($\langle ij \rangle$) that are nearest neighbors, and $a_i^\dagger$ (a_i) are creation (annihilation) operators. In the absence of disorder, the bandwidth is tuned by t_{ij}. The lack of mini-band formation in nanocrystal superlattices that are separated by organic ligands[6] stems from the small electronic coupling (t_{ij}) due to the long insulating organic ligands. This small electronic coupling is dominated by the site energy disorder ($\delta\varepsilon_i$) that is a result of the size dependent band gaps of nanocrystals. Further the ligands can stabilize a ploaronic state within an individual nanocrystal further constraining charge transport.[7] To increase t_{ij}, neighboring nanocrystals must be close and have a low potential barrier. Short organic and inorganic linkers have been used to replace the long insulating ligands;[8,9] however, the transport in these materials is often dominated by a hopping mechanism,[10–12] indicating t_{ij} is still too small relative to $\delta\varepsilon_i$.

One way to further increase t_{ij} is to eliminate the high band gap molecular species between the nanocrystals and form a homoepitaxial bridge between crystallographically aligned nanocrystals.[13] In essence, a thin neck between nanocrystals maintains individual quantum confinement while allowing for sufficient electronic communication. A prototypical example of this is the formation of well-ordered square and honeycomb superlattices of attached PbX (X=Se,S,Te) nanocrystals.[14–16] Unfortunately, these materials still show hopping transport (although with quite high mobilities[17]) despite theoretical predictions of mini-band states (*i.e.* t_{ij} is sufficiently large compared to $\delta\varepsilon_i$).[15,18] The reason for the lack of mini-bands appears to be that the variations of the on-site energy ($\delta\varepsilon_i$) and coupling strengths (δt_{ij})

between neighboring nanocrystals are still too large, resulting in Anderson-like localization.[5,15,19]

There are three structural parameters that can cause disorder in the energy landscape and, thus, must be controlled: the nanocrystal size distribution ($\delta\varepsilon_i$), the dot-to-dot spacing (δt_{ij}), and the thickness of the homoepitaxial neck (also δt_{ij}). The first is addressed by using nanocrystals with narrow size distributions, and subsequent small site energy disorder. Considerable strides have been made to minimize disorder in dot-to-dot spacing in PbSe superlattices,[20] addressing the second source of disorder. Yet to be addressed are neck thickness variations, which contribute more to carrier localization than positional disorder.[15] These neck thickness variations are considerable,[20] and subsequently lead to large variations in the nearest neighbor coupling strength.[21] Unfortunately, it is unclear if improved uniformity of the neck thickness can be achieved in attached PbX superlattices. Specifically, neither subsequent layer by layer growth of additional material nor annealing of PbX superlattices appears to remove neck thickness variation.[22,23] Therefore, the electronic coupling being controlled by a thin bridge of material between the nanocrystals is an inherent problem with this design as it is ultimately difficult to control this parameter. Thus, we developed a clean sheet redesign of atomically attached nanocrystal superlattices which inherently eliminates neck thickness issues and presents other opportunities for tuning the coupling and on-site energy.

Results and Discussion

Synthetic Design

We propose to make 2D quantum dot (QD) superlattices based on composition variations. The goal is for the intrinsic properties of the QD and matrix material (band offsets, effective masses, dielectric constants) to control the coupling. We build off of our previous *in-situ* TEM studies where we identified atomic attachment of hexagonal prism shaped

wurtzite CdSe nanocrystals on $\{1\bar{1}00\}$ facets minimized harmful defects.[24] From this we identify hexagonal prism shaped CdSe/CdS core/shell nanocrystals terminated with $\{1\bar{1}00\}$ facets[25,26] (Figure 1a) as an ideal building block to prepare atomically attached nanocrystal superlattices based on composition variations. Hexagon shaped nanocrystals have an additional advantage of interlocking, likely helping achieve well-ordered superlattices.

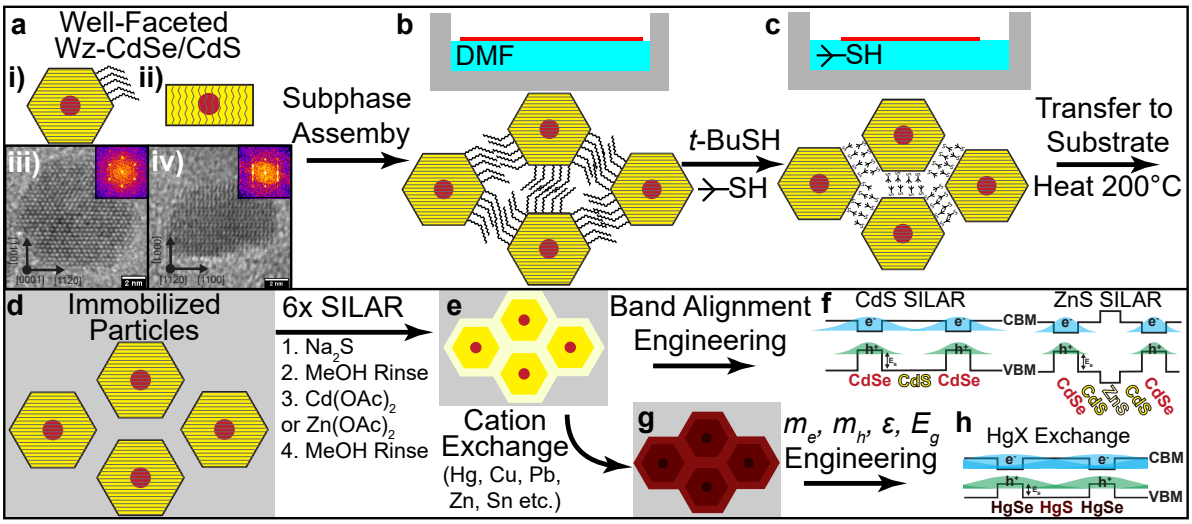

Figure 1: Scheme for assembling and attaching wurtzite CdSe/CdS core/shell nanocrystals into crystallographically fused arrays (a) Schematic representation of the prepared CdSe/CdS core shell nanoplatelets viewed down the (i) $\langle 0001 \rangle$ zone axis and (ii) the $\langle 11\bar{2}0 \rangle$ zone axis with representative HRTEM images (iii) and (iv) respectively. (a) DMF liquid subphase assembly of CdSe/CdS nanocrystals into hexagonal ligand separated superlattices followed by (c) *in-situ* ligand exchange to *t*-BuSH. (d) Transfer of *t*-BuSH terminated superlattices to substrate followed by a 5 min 200°C anneal to thermally decompose the ligands. (e) SILAR treatment to epitaxially grow bridges between the particles. (f) Schematic energy band alignment for CdSe/CdS/CdS and CdSe/CdS/ZnS prepared by assembly and subsequent SILAR. (g) Cation exchange to other II-VI and IV-VI materials to (h) engineer desired semiconductor properties (*i.e.* delocalization).

Figure 1 outlines our scheme to prepare 0D-2D QD-in-matrix superlattices. We start with colloidal hexagonal prism shaped CdSe/CdS core/shell nanocrystals (Figure 1a) terminated with $\{1\bar{1}00\}$ facets (full characterization in Figure S1 and Figure S2). The nanocrystals self assemble on a liquid subphase[27] into 2D hexagonal superlattices with their c-axis perpendicular to the substrate (Figure 1b), resulting in face-to-face alignment of the $\{1\bar{1}00\}$ facets. Next, the native oleate ligands are replaced with *t*-BuSH (Figure 1c),[28] the nanocrystals are

transferred to a substrate, and annealed to decompose the organic ligands (Figure 1d) which locks in the superlattice structure. Layer by layer growth of iso-structural material[29] (Figure 1e) attaches the nanocrystals and can engineer band alignments in the 2D superlattice enabling quasi-type II and type I alignments in the case of CdS and ZnS, respectively (Figure 1f). The semiconductor properties can be further engineered by cation exchange conversion (Figure 1g) to modulate semiconductor properties (Figure 1h). Using this method, we achieved superlattices with multiple μm sized single crystal-like atomic domains and well-ordered CdSe QDs within the CdS matrix. Importantly, we achieve uniform neck thicknesses upon thermal annealing, resulting in a uniform electronic coupling landscape (*i.e.* small δt_{ij}). Lastly, we demonstrate the CdSe/CdS arrays can be transformed into HgSe/HgS arrays *via* cation exchange. Our results present a general and tuneable method for preparing 0D-2D nanocrystal superlattices of II-VI semiconductors.

Superlattice Structure

Initial assemblies of oleate capped nanocrystals are prepared by evaporating dilute octane solutions of nano-hexagonal prisms on a DMF liquid subphase in a teflon well. Figure 2a-i shows a model of the oleate separated superlattices. In Figure 2a-ii high angle annular dark field scanning transmission electron microscopy image (HAADF-STEM) of the superlattice, which has linear thickness contrast, demonstrating the lack of inorganic material bridging the nanocrystals. In Figure 2a-iii, a bright field TEM image shows similar well-ordered structures. HRTEM of the native lattice shown in Figure 2a-iv show the $\{1\bar{1}00\}$ facets of the hexagons are matched face to face separated by the space occupied the oleate ligands. Figure 2a-v shows a small angle electron diffraction pattern, collected over an 11 μm^2 area. The hexagonal spots, consistent with a single crystal hexagonal superlattice domain, indicate the samples preserve the structure observed in Figure 2a-iii across large length scales. Specifically, Figure S3 shows that we can obtain single superlattice domains of at least 7 μm by 7 μm (49 μm^2). Wide angle electron diffraction in Figure 2a-iv shows peaks correspond-

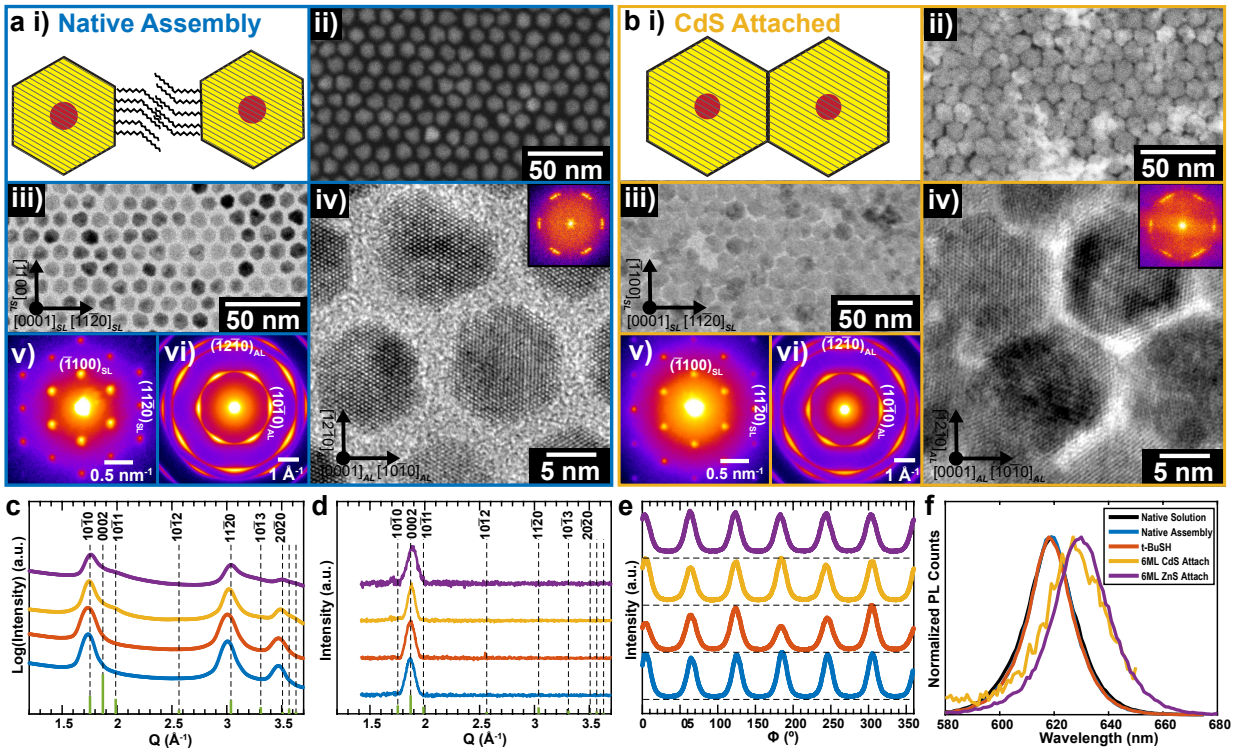

Figure 2: Structural characterization of assembled and attached superlattices. (a) native assembly of CdSe/CdS dots, and (a) after growing 6ML of CdS *via* SILAR. i) schematic of the assembly, ii) HAADF STEM image, iii) bright field TEM, iv) HRTEM, v) small angle selected area electron diffraction and vi) wide angle selected area electron diffraction both collected over an $11\mu m^2$ area. (c) radially integrated wide angle-SAED, (d) wide angle x-ray diffraction ($\theta - 2\theta$ geometry) (e) azimuthal integrated wide angle-SAED of the $\{1\bar{1}00\}$ diffraction peak, and (f) normalized photoluminescence for Native (blue), *t*-BuSH treated (red), 6ML of CdS SILAR (yellow), 6ML ZnS SILAR (violet), and solution suspended dots (black, PL only).

ing to $\{1\bar{1}00\}_{AL}$, $\{11\bar{2}0\}_{AL}$, and $\{2\bar{2}00\}_{AL}$ planes of the wurtzite lattice, indicating that the nanocrystals are oriented with their c-axis perpendicular to the substrate and have in-plane orientational order. The arcs rather than spots indicate that there is variation in the atomic lattice orientation in-plane within the sample. These structures are similar to aligned bi-pyramid and bi-frustum ZnS nanocrystals previously reported.[30,31] Taken together, the TEM and diffraction data suggests that we have prepared monolayer hexagonal superlattices of wurtzite CdSe/CdS nano hexagonal prisms where the nanocrystals share a common crystal alignment.

The superlattice structure is maintained during *in-situ* ligand exchange[32] to place *t*-

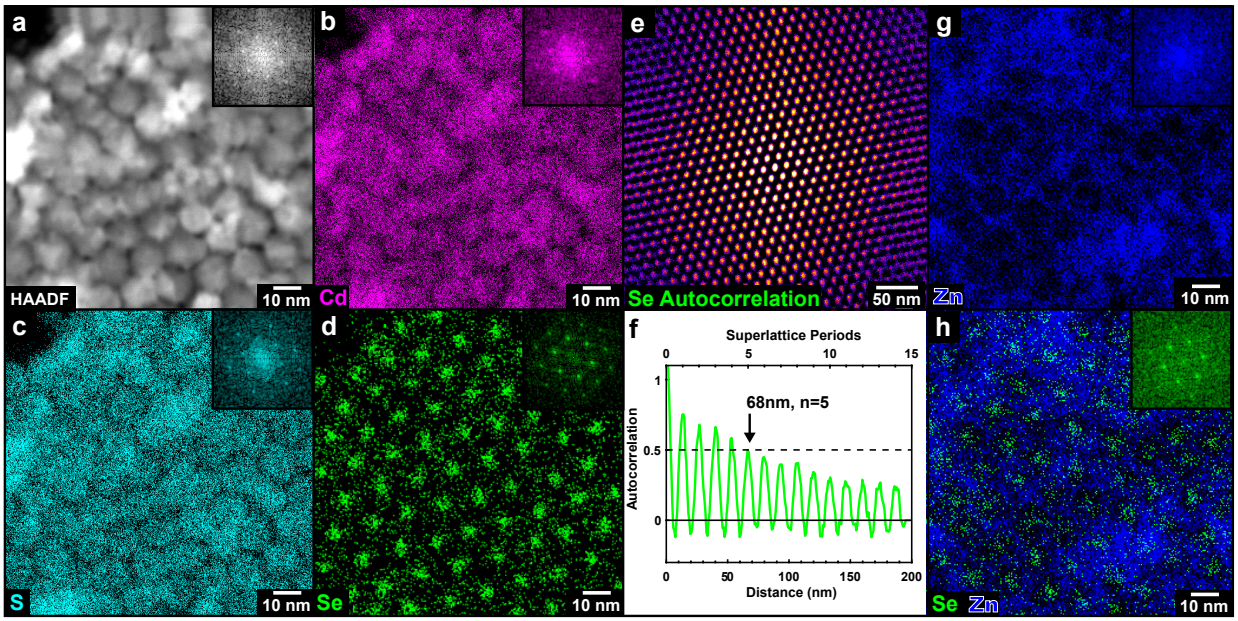

Figure 3: Elemental mapping of superlattices. (a) High angle annular dark field STEM signal, (a) cadmium L, (c) sulfur K, and (d) selenium K signal for a CdSe/CdS array with 6 monolayers of SILAR grown CdS at the interface. (e) 2D autocorrelation function of the selenium signal for a large area selenium map (see Figure S16) and (f) a linecut along the $\Gamma - M$ ($[11\bar{2}0]_{SL}$) direction. (g) Zinc K signal and (h) selenium K signal from a CdSe/CdS sample with 6 monolayers of SILAR grown ZnS at the interface.

BuSH on the surface, transfer to substrates, and thermal annealing to remove the surface ligands, except the superlattice parameter (QD-QD spacing) decreases slightly (Figure S4b and Figure S8) indicating a topotactic transition similar to Abelson *et al.*.[33] Substrate supported ligand free nanocrystals (see Figure S7 for FTIR confirmation) are used as templates to subsequently grow CdS and ZnS layers[29] to bridge the nanocrystals. We note the *t*-BuSH treatment and annealing is critical for maintaining order during subsequent SILAR treatments (Figure S5). In Figure 2b, a superlattice after 6 cycles of CdS SILAR is shown. From the HAADF STEM in Figure 2b-ii, we observe quite uniform STEM signal indicating uniformly thick inorganic material, highlighting successful bridge formation. Further evidence for the successful infilling of the bridges is the decrease of the small-angle electron diffraction amplitude (Figure S8). TEM(Figure 2b-iii), HRTEM (Figure 2b-iv), and wide angle electron diffraction (Figure 2b-vi) indicate homoepitaxial growth of wurtzite CdS in the bridges. Small angle diffraction in Figure 2b-v indicate large area superlattice domains

remain. We don't observe any obvious effects from the substrate (amorphous carbon) affecting the SILAR growth, however use of crystalline substrates may present interesting future opportunities. Similar results are observed for heteroepitaxial growth of ZnS as the bridge material (see Figure S4d) highlighting the generality of this approach. There can be considerable strain due to the lattice mismatch of CdSe, CdS and ZnS, which may prove difficult to address in films which tile all space, currently though, attachment induced defects likely provide stress relief. Finally, the core-to-core spacing can be tuned by modulating the initial shell thickness, for example CdSe cores with thinner 4ML shells result in superlattices with a smaller (8.5 nm *vs.* 12 nm) spacing (Figure S6).

Radially integrated wide angle electron diffraction patterns for all samples (Figure 2c) taken in transmission geometry show diffraction intensity from $\{hki0\}$ peaks, consistent with the c-axis normal to the substrate (see Figure S9 for diffraction geometry). Diffraction patterns collected in $\theta - 2\theta$ geometry (from a $\sim$1 cm^2 substrate) show only the $\{0002\}$ diffraction peak (Figure 2d), further supporting the perpendicular c-axis orientation over large areas. Azimuthally integrating the $\{1\bar{1}00\}$ peak (Figure 2e) reveals 6 distinct peaks indicating strong in-plane orientational order. We measured the full width at half max for each sample and found no additional broadening throughout processing (Table S1) indicating the attachment strategy does not introduce additional in-plane orientational order and is comparable to atomic attached PbX Materials (Table S2). Further we have observed the superlattice and atomic lattice ordering is maintained in the z-direction of bi-layer (Figure S11, Figure S12, Figure S13) and multi-layer (Figure S14) samples indicating this strategy may allow for epitaxy in 3 dimensions. Taken together the TEM and diffraction data indicate minimal disruption to superlattice structure, order, or atomic alignment during attachment of the nanocrystal assemblies.

Importantly, room temperature photoluminescence from the attached samples (Figure 2f) indicate the quantum confined 0D CdSe core is maintained. Comparing CdS bridges to ZnS bridges, we qualitatively observe brighter band edge PL from the ZnS sample, con-

sistent with confinement of both carriers in the ZnS infilled case. Interestingly, we observe a ∼5 nm redshift in both CdS and ZnS infilled samples, which is unexpected. Less redshift is expected in the strongly confined ZnS case and electronic structure calculations from CdSe/CdS dimers bridged with CdS and ZnS respectively support this (see Figure S20). This suggests additional factors may dictate PL redshifts (see SI for discussion). The PL intensity (Figure S10A) from the CdS SILAR samples is considerably lower compared to the initial assemblies or the *t*-BuSH treated samples. Additionally, the ZnS case is noticeably brighter than the CdS SILAR case. Qualitatively this indicates additional non-radiative pathways have been introduced upon SILAR fusion which time resolved photoluminescence lifetime measurements also suggest (Figure S10B). Indeed engineering the bridge material can produce a material with optimal band alignments for luminescence (*i.e.* CdSe/CdS/ZnS type I) or electronic overlap (*i.e.* CdSe/CdS/CdS quasi-type II).

To probe the structural properties of the CdSe cores (the "artificial atoms"), we use STEM-EDS elemental mapping to resolve elemental distributions in our samples. Figure 3a-d shows the HAADF, Cd, S, and Se signal respectively. In the case of the Se, we observe a well-ordered hexagonal lattice, indicating that the self assembly preserved the underlying compositional heterostructure encoded in the initial CdSe/CdS nanocrystals (composition analysis shown in Figure S15). To quantify the ordering over larger length scales, we collected large field of view STEM-EDS maps (Figure S16) and calculated the 2D autocorrelation function of the Se signal (Figure 3e). The fact that the amplitude slowly decays over large distances is indicative of a well-ordered sample. Specifically, a linecut along the $\Gamma - M$ ($[11\bar{2}0]_{SL}$) direction (Figure 3f) shows that the amplitude is damped to 50% (defined as $\xi_{0.5}$ by Pichler *et al.*[34]) of its original values at 68 nm or 5 superlattice repeat units. The ordering achieved here is considerably better than the best ordered SK-grown 2D QD superlattices and comparable to optimized direct atomic attachment cases (Table S3). In the case of heteroepitaxial growth, we observe a faint honeycomb structure in the the Zn signal indicating the ZnS (Figure 3g) was preferentially the bridge material between the nanocrystals, and

the CdSe is localized inside the ZnS honeycomb (Figure 3h). Taken together, we have thus presented a modular approach for growing 0D-2D hybrid semiconductor heterostructures.

Understanding Effect of Structural Parameters on Electronic Coupling

Thus far, we have shown that our strategy can prepare superlattices of CdSe QDs in a CdS matrix. Next, we aim to understand the electronic coupling in these materials and the effects of disorder in the system. To this end, we performed electronic structure calculations using the semi-empirical pseudopotential method[35,36] on dimers and trimers of epitiaxially connected CdSe/CdS nanocrystals. This computational method accounts for strain effects by utilizing molecular dynamics based structural minimization and has been shown to be in quantitative agreement with experimental measurements (consult the methods section for details).[37,38] We note that experimentally we observe in-plane orientational disorder (*i.e.* tilts) and these are not considered in our calculations. We observe localization of the holes to the CdSe cores due to the large valance band offset (Figure S18). The electron states are shared between the two nanocrystals as seen by electron density in the neck region (Figure S18) due to the small conduction band offset and light effective mass of electrons in these materials.

We quantify the coupling (t_{ij}) between the electron states by using energy splitting of the "bonding", σ-like state (symmetric addition of $1S_e$ states) and the "antibonding", σ^*-like state (anti-symmetric addition of $1S_e$ states). Calculations were performed for which we independently varied the distance between the cores (*i.e.* bond length) and the thickness of the neck (see methods and Figure S21 for visualization of select structures). In Figure 4a, we observe that as the core spacing increases, the coupling strength decreases, and there is a corresponding decrease in electron density at the interface (Figure 4b). This variation in tunnel splitting with dot-to-dot distance represents the effects of positional order on the energetic disorder in our samples. Next, we study the dependence of the tunnel splitting

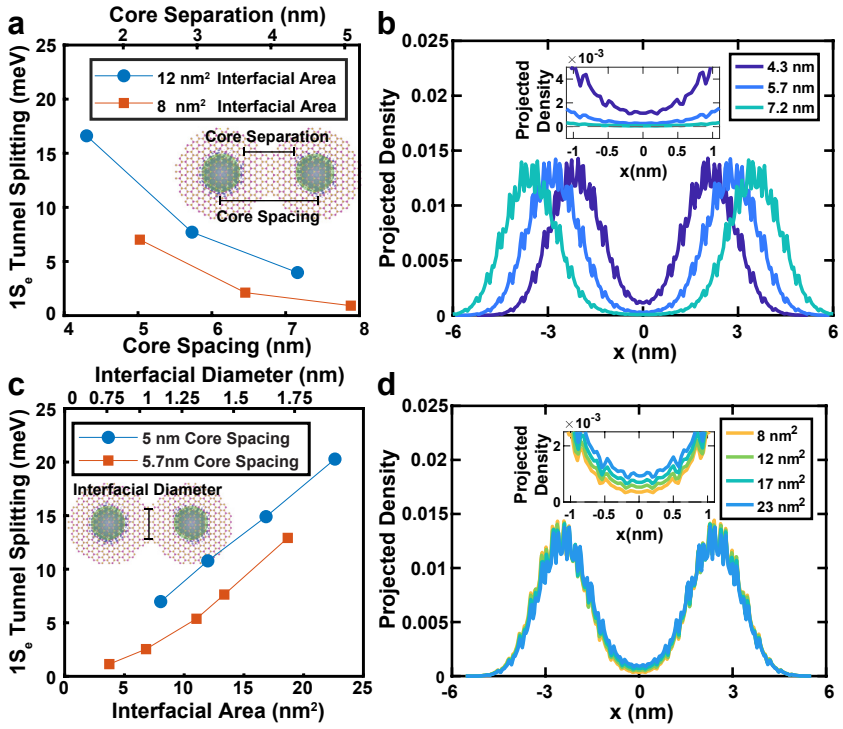

Figure 4: Electronic structure calculations of coupled CdSe/CdS QDs. (a) Tunnel splitting of the electron $1S_e$ states as a function of the core separation between CdSe/CdS nanocrystal dimers with fixed interfacial areas. (b) The projected electron densities for the 12 nm^2 interfacial area calculations of (a) with the insets showing how the larger tunnel splittings results in larger electron density at the origin (*i.e.* in the middle of the two nanocrystals). (c) Tunnel splitting of the electron $1S_e$ states as a function of the interfacial area between two attached CdSe/CdS nanocrystals with fixed core spacings. (d) Projected electron densities for the 5 nm core spacing nanocrystal dimers of (c) with the insets showing how larger interfacial areas results in more electron density as the origin.

variation on the neck thickness (Figure 4c). In this case, we find that the tunnel splitting increases as the interfacial area (A) increases with a power dependence between $A^{1.0}$ and $A^{1.5}$, in close agreement to the power dependence of $A^{3/2}$ previously predicted by effective mass models.[21] This strong dependence of the coupling strength on interfacial area indicates that this may be the dominant factor contributing to the energetic disorder.

As predicted from our calculations, and suggested by Whitham *et al.*,[15] neck thickness variation can be the dominant factor causing energetic disorder. In the PbX systems typically explored, thin necks are necessary to preserve quantum confinement and they must be uniformly sized to achieve consistent coupling strengths. Unfortunately, post synthetic

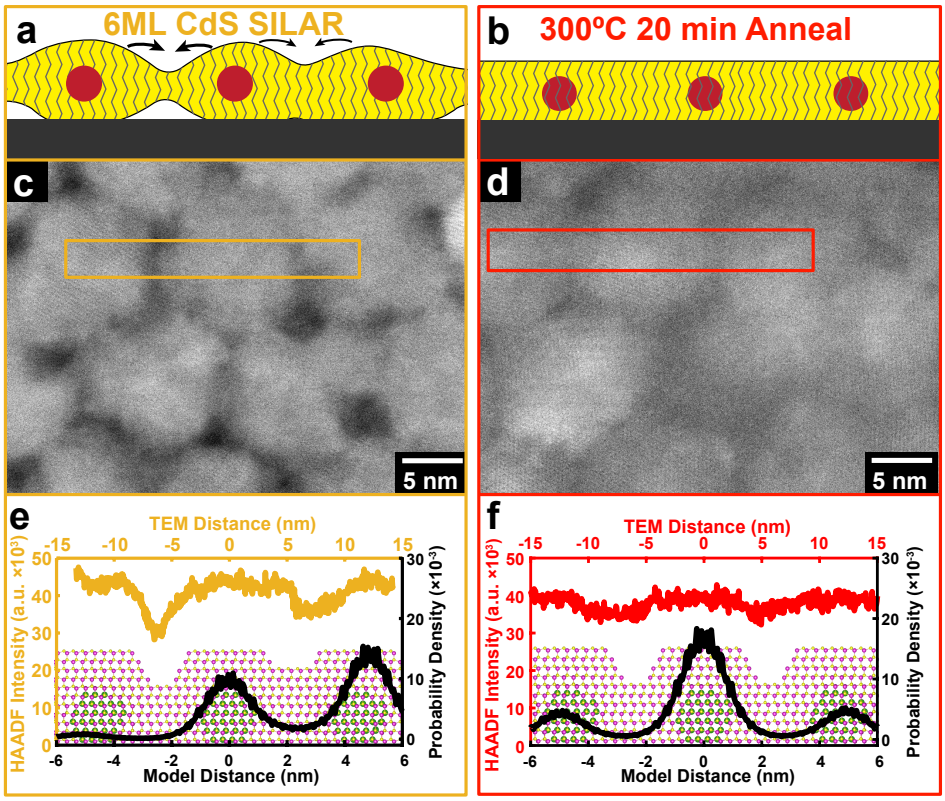

Figure 5: Annealing to minimize thickness variations. (a) Schematic of 3 fused CdSe/CdS nanocrystals viewed down the $\{11\bar{2}0\}$ zone axis with inhomogeneous neck thicknesses initially and (b) after thermal annealing. HAADF STEM image of (c) an initial CdSe/CdS superlattice with 6 monolayers of SILAR CdS grown at the interface and (d) after annealing for 20 min at 300°C in flowing argon. HAADF intensity profile (top) for (e) for the 3 merged particles in the yellow box and (f) for 3 merged and annealed particles in the red box. Electron densities of the LUMO state projected onto the attachment axis overlayed on the nanocrystal trimers with (e) asymmetric neck thicknesses and (f) symmetric neck thicknesses used in the atomistic electronic structure calculations.

growth of additional material does not decrease the thickness variations.[22] In our system, we have encoded the QD potential using anion composition variation, and thus a film of uniform thickness can be made while maintaining the 0D quantum confinement. We analyze the neck thickness variations in our samples with SILAR grown CdS at the interface using HR-STEM imaging which has linear thickness contrast. Figure 5a,c shows the initial CdSe/CdS superlattice with non-uniform neck thicknesses. In Figure 5e, we show a line-scan of the interface between 3 particles in the yellow box highlighting the non-uniform thickness. The inset model is a linear trimer of equidistant CdSe/CdS nanocrystals, with single

atomic layer variations in their neck thicknesses. The lowest lying electron state (Figure 5e black) is localized on the dot with the thicker bridge indicating that Anderson-like localized states result from neck thickness variations. After annealing the sample at 300°C for 30 min, surface diffusion of CdS preferentially infills the voids which are thinner, resulting in films of uniform thickness (Figure 5b, d). A line-scan across 3 particles in red (Figure 5f), shows the uniform thickness of the bridges. In this case, the electronic structure of an equidistant linear trimer with uniform neck thicknesses recovers the linear H_3-like molecular orbitals (see Figure S19 for more states) which translates to electronic bands in the infinite chain limit. We note that the uniform thickness also indicates the thickness of the CdS shell is uniform throughout, which is important for achieving uniform site energies (Figure S22). Importantly, the slow interdiffusion on the anion sublattice in II-VI materials preserves the 0D CdSe cores throughout the annealing process (Figure S23).

Cation exchange to access additional compositions

The exquisite synthetic control achieved in CdX semiconductor nanocrystals has enabled the hexagonal prism shapes critical for atomic alignment. Nonetheless, it would be desirable to access additional semiconductors to control properties (*i.e.* m_e, m_h, spin-orbit coupling, *etc.*) more precisely. Shape controlled colloidal nanocrystals of desirable synthetic targets often are not available, however cation exchange in semiconductor II-VI materials can expand the chemical diversity of semiconductor nanostructures with exquisite control.[39] Herein we demonstrate one possible conversion, CdSe/CdS to HgSe/HgS *via* a two step exchange. We target HgX materials since they have light carriers, facilitating greater delocalization.[40] Importantly, the structure aspects which we have engineered in CdSe/CdS superlattices are maintained throughout the transformations.

In detail, we start with wurtzite CdSe/CdS superlattices (Figure 6a) and use tetrakis (acetonitrile) copper(I) hexaflurophosphate in methanol to convert the sample to $Cu_{2-x}Se/Cu_{2-x}S$. STEM EDS quantification (Figure S26) shows the removal of cadmium. Upon treatment

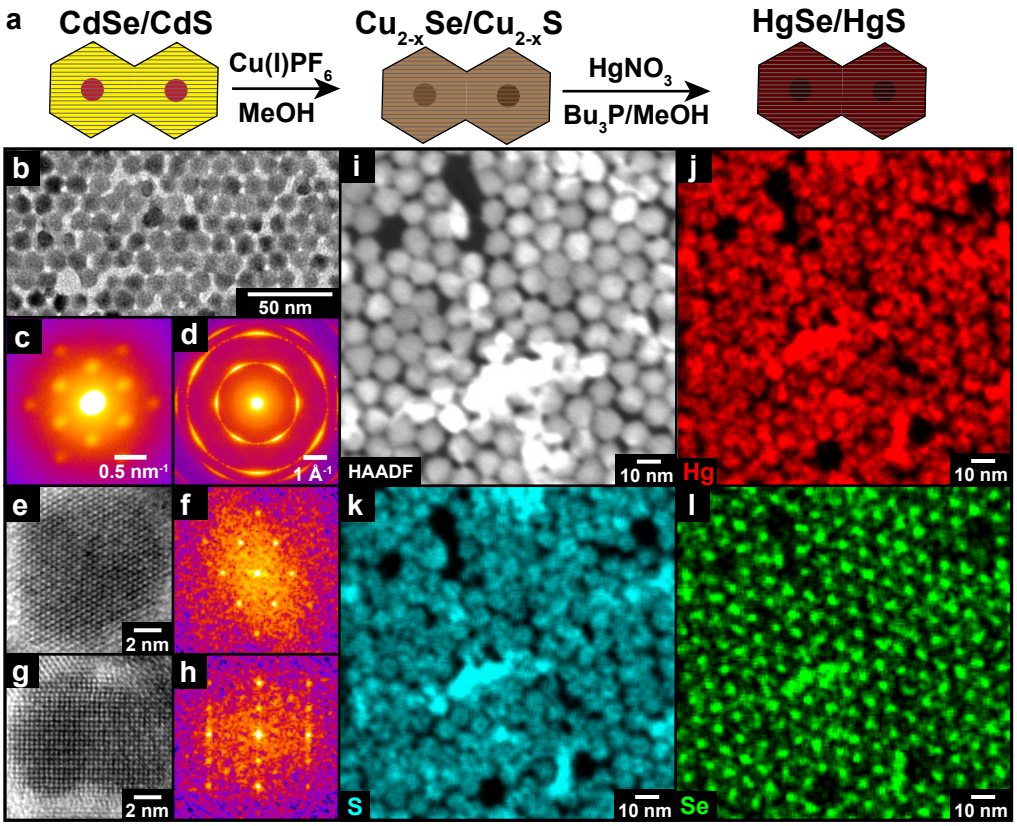

Figure 6: Cation exchange to prepare HgSe/HgS superlattices.(a) schematic for converting CdSe/CdS superlattices to HgSe/HgS *via* a $Cu_{2-x}Se/Cu_{2-x}S$ intermediate. (a) TEM image, (c) small angle and (d) wide angle electron diffraction of a HgSe/HgS superlattice. (e) HRTEM image and (f) corresponding Fourier transform of a single HgSe/HgS particle within a superlattice viewed down the $\langle 0001 \rangle$ zone axis. (g) HRTEM image and (h) corresponding FT viewed down the $\langle 11\bar{2}0 \rangle$ zone axis. (i) HAADF, (j) mercury L, (k) sulfur K, (l) and selenium K maps for a HgSe/HgS superlattice.

with $Hg(NO_3)_2$/tri-butlyphosphine, EDS indicates near complete conversion to HgSe/HgS (Figure S27). The ordered structure of the superlattice is maintained as confirmed by TEM and small-angle SAED (Figure 6b,c). Wide angle transmission electron diffraction shows a wurtzite[0001]-like single crystal diffraction pattern similar to the initial samples, indicating that the atomic ordering is maintained in the system.[41] HRTEM images of the particles viewed down the c-axis (Figure 6e,f) show a hexagonal atomic structure, and a particle viewed edge on (Figure 6g,h) show a wurtzite-like atomic structure.[42] Furthermore, elemental maps of the Hg, S, and Se (Figure 6i-l) show that the well-defined and ordered Se cores are maintained throughout the exchange. Thus, cation exchange allows us to utilize the ma-

terials with the best synthetic control (*e.g.* CdSe/CdS QDs) for assembly and easily switch to a desired functional material, as demonstrated herein with a CdSe/CdS to HgSe/HgS reaction.

Comparison of NC assembly/SILAR attachment with direct atomic attachment

In this work, we have presented an approach for bottom-up fabrication of atomically attached nanocrystal superlattices that addressed some key shortcomings of direct attachment strategies. By completely separating the nanocrystal assembly and attachment in this work, we achieved better control over the attached superlattice structure enabling large grain size assemblies. However by locking the superlattice geometry on a substrate, we also encode less ideal structural characteristics. For example, there is considerable in-plane orientational disorder in our samples, $\Phi_{\{1\bar{1}00\}} \sim 15^{\circ}$, which indicates the nanocrystals have imperfect alignment relative to each other. Upon attachment, this angular coherence does not improve (Table S1). In the case of direct atomic attachment of nanocrystals, during the concerted assembly and attachment process, nanocrystals are free to rotate on the liquid interface during the attachment process, which increases the likelihood of high quality attachment and low angular misorientation. Indeed, attached PbSe systems have achieved better angular coherence to date (Table S2) indicating that the greater control of the SILAR attachment method has limited the system's ability to relax potentially unwanted misorientation. Ultimately a better understanding of the source of angular misorientation in the presented systems will identify assembly, attachments, and/or post processing strategies to allow greater freedom for nanocrystals to avoid angular misorientations.

Next, we consider transformations of the superlattice structure that occur during attachment of the nanocrystals in our SILAR method and the direct atomic attachment routes. In our work, the symmetry and nanocrystal positions in the unit cell are unchanged (*i.e.* hexagonal to hexagonal transition). In this case, we can leverage the diversity of ligand separated

nanocrystal superlattices to achieve attached nanocrystal superlattice structures. In the case of PbX assembly and attachment, the initial ligand separated nanocrystals typically adopt a hexatic phase, and, in the case of monolayers, typically transform to a square superlattice upon attachment.[43] This requires concerted shuffling of nanocrystals, and the kinetics of this process must be carefully controlled to achieve well-ordered square superlattices. Indeed this complex interplay results in a diversity of structures including residual hexatic order,[44] distorted square superlattices,[43] or in the case of bi-layers more complex silicene structures.[45] Indeed the structural diversity as a result of small tweaks to direct attachment of PbX is intriguing and has potential to yield diverse structures. Unfortunately though, this also makes the system sensitive to small perturbations, and thus reproducible and deterministic synthesis of a desired structure is difficult. Ultimately the improved superlattice structural control of the nanocrystal assembly/SILAR attachment approach, comes at the expense of individual nanocrystal freedom enabling tighter atomic alignment.

Electronic coupling between the nanocrystals

A brief discussion on the tunability of the direct electronic coupling between the nanocrystals (t_{ij} matrix elements in Eq. 1) is justified. In contrast to the PbX superlattice family, we have shown that the QD-in-matrix superlattices presented here can be made to have homogeneous neck thicknesses and, consequently, homogeneous electronic coupling strengths. The magnitude of the homogeneous electronic coupling being controlled by the bulk effective masses and band alignments of the valence and conduction bands between the component materials. Specifically, the lighter the effective mass of the carrier and smaller the band offset between the core, shell, and SILAR materials, the larger the magnitude of the electronic coupling. Overall the coupling in these systems can be strengthened by converting (*e.g. via* cation exchange) to light effective mass semiconductors such as HgSe/HgS ($m_{e(HgSe)} = 0.05m_0$ and $m_{e(HgS)} = 0.03m_0$) compared to CdSe/CdS ($m_{e(CdSe)} = 0.13m_0$ and $m_{e(CdS)} = 0.21m_0$). The impact of the band offset can be seen by noting that the large valence band

offsets between CdSe and CdS leads to negligible electronic coupling in the valence band (sub 1 meV) which is considerably smaller than the electronic coupling in the conduction band ($\sim$ 15 meV) (Figure 4). Additionally, a prudent choice of the materials can modulate the direct electronic coupling in the conduction band. For example, the conduction band coupling can be reduced by using ZnS as the SILAR material instead of CdS (Figure S20). Together the diverse materials systems demonstrated here provide ample knobs to tune the direct electronic coupling landscape for the desired properties.

Interestingly, near field coupling of the crystallographically oriented quantum dots presents additional considerations and opportunities. For example, considering energy transfer in these arrays, the mutual orientation of dipoles can modulate (enhance) energy transfer (*i.e.* increase κ^2 in FRET). Further, optically excited nanocrystals interact with one another through the radiation field which can result in drastic changes to the optical response of quantum dot assemblies compared to isolated emitters.[46] A critical aspect for these collective phenomena is the spontaneous alignment of the transition dipole moment. As an example, superflourescence has been observed in $CsPbBr_3$ nanocrystal superlattices where a strong laser field leads to correlated dipoles.[47] The low symmetry of the wurtzite lattice and the high quality positional and orientational order may further enhance these effects. The materials presented in this work may permit optical experiments where the electronic coupling, radiative coupling, and dipole orientations can be independently tuned. The flexibility will identify critical parameters and thus help develop design rules for observing collective optical behavior in quantum dots superlattices.

Conclusion

The combination of colloidal synthesis and self assembly with solution phase epitaxial growth techniques results in tunability that affords materials with independent structural control of final hybrid 0D-2D nanomaterials. Importantly, we demonstrate a viable strategy to elimi-

nate inhomogeneous neck thicknesses, which are known to cause Anderson-type localization and have been a primary hindrance to the realization of collective phenomena in quantum dot superlattices. The generality of this method allows for independent modification of the core material, shell material, bridge material, and the band alignments. In addition, the modularity affords the possibility of using traditional materials growth (*e.g.* MOCVD, MBE) to grow the inorganic bridges, presenting innumerable material combinations for artificial 2D lattices. Finally, the large single (super)crystal domains demonstrated here (multiple μm) are ripe for single domain transport or optical studies, enabling domain level understanding of QD-in-matrix superlattices and eventually nanotechnologies enabled by artificial lattice properties.

Methods/Experimental

Materials: Cadmium oxide (CdO) 99.99% Aldrich; oleic acid 90% (OA) technical grade Aldrich; oleylamine (OAm) technical grade 70% Aldrich; octadecene 90% (ODE) technical grade Aldrich; trioctylphosphine oxide (TOPO) 99% Aldrich; Sulfur Aldrich; Octadecylphosphonic Acid (ODPA) 99%, PCI Synthesis; *n*-trioctylphosphine 97% (TOP) Strem; *t*-BuSH Aldrich *n*-tributylphosphine Strem; $Hg(NO_3)_2$ Aldrich; tetrakis(acetonitrile) copper(i) hexaflurophosphate Aldrich; anhydrous Na_2S Strem; methanol 99.5% extra dry Acros; selenium 99.99% Strem; 0.2M $Cd(oleate)_2$ in ODE was prepared by degassing appropriate amounts of CdO, OA, and ODE under vacuum at 110°C at until all gasses and water had evolved. The flask was switched to argon and heated to 240°C until a clear (slightly yellow) solution solution was obtained. The flask was then cooled to 110°C and degassed a second time to remove additional water.

Wurtzite CdSe Seeds: CdSe cores were synthesized using a modified version of a previously published procedure.[48] Typically, 120 mg of CdO, 560 mg of ODPA, and 6 g of TOPO were combined and degassed at 150°C under vacuum for one hour. The reaction was

then heated to 320°C under argon, and held at that temperature until the solution turned clear, indicative of Cd-ODPA complexation. At 320°C, 3 g of TOP was injected, and then the solution was heated to 360°C, at which point a solution of Se (120 mg) dissolved in TOP (0.72 g) was quickly injected. The reaction was stopped after approximately 4 min, and quickly cooled. Changing reaction temperature and reaction time allows for synthesis of different-sized cores. In this work we used large CdSe cores to facilitate STEM EDS identification, typical 1st exciton absorption was ∼570 nm. The QDs were purified from free ligand and excess precursors *via* precipitation with acetone and redispersion in hexanes several times. Sizing and concentrations were determined using previously established calibration curves.[49]

$\{1\bar{1}00\}$ Terminated Hexagon Shaped CdSe/CdS Core Shell Nanoplatelets: Samples with a nominal shell thickness of 6 monolayers were synthesized based on heavily modified previous procedures[50] as follows. 100 nmol of wurtzite CdSe seeds (570 nm 1st exciton), 3 ml ODE and 3 ml OAm were loaded into a 50 ml 3 neck round bottom flask and degassed at 110°C for ∼30 min. Under Ar, the reaction was heated to 310°C. At 240°C, slow injection of a 3.14 ml of 0.2 M Cd(oleate)$_2$ in ODE solution and 3.14 ml of 0.2M TOP-S solution in TOP in separate syringes commenced at a rate of 1ml/hr. TOP-S in TOP was prepared by stirring 20 mg of S in 2.6 g TOP in a glovebox for ∼ 30 min. After the injection completed, the reaction was kept at 310°C for 10 min and then rapidly cooled to room temperature. Nanocrystals were isolated from the reaction by precipitating the nanocrystals with acetone and redissolving in hexanes 2×. Finally the nanocrystals were centrifuged at 8000 rpm in hexanes to remove any remaining insoluble impurities. Samples were stored in a N_2 glovebox and small aliquots were removed for subsequent self assembly experiments

Nanocrystal Assembly: Monolayer nanocrystal superlattices were prepared at the liquid-air interface.[27] Briefly, 1 ml of anhydrous DMF was placed in a 1cm^2 square teflon well. Next CdSe/CdS hexagonal platelets were diluted in octane to an appropriate concentration to achieve monolayer coverage and 100 μl of the diluted nanocrystal solution in octane was floated on top of the DMF layer. The well was covered with a glass slide to slow solvent

evaporation, and was allowed to sit for at least 8 hours. Subphase ligand exchange[32] with *t*-BuSH was performed by slowly and carefully injecting 100 μl of a 0.17 mM solution of *t*-BuSH in DMF into the DMF subphase. The sample was allowed to sit for $\sim$2 hours with the *t*-BuSH/DMF subphase. The samples were transferred *via* scooping from below to the desired substrate (amorphous carbon coated TEM grid for microscopy or a glass coverslip for X-ray diffraction and spectroscopy) for further processing. Samples were placed in a vacuum oven under house vacuum at $\sim$ 50°C to remove any remaining subphase solvent. Next the samples were placed on a glass slide and placed on a 200°C hotplate in air for 5 min to thermally decompose the *t*-BuSH. We found that this step could be performed in air without noticeable deleterious effect on the structure or properties of the samples.

SILAR Attachment: Successive ion layer adsorption and reaction (SILAR) was performed in a N_2 glovebox with anhydrous solvents. 20 mM stock solutions of anhydrous Na_2S in MeOH and 20 mM $CdOAc_2$ in MeOH were prepared. A sample after the above described *t*-BuSH treatment was loaded into self closing anti capillary tweezers and sequentially dipped in the Na_2S solution for 30 s, then a neat MeOH rinse for 30 s, then the $CdOAc_2$ solution for 30 s, and finally a second MeOH rinse which was separate from the first rinse solution. This process constitutes 1 mono-layer of SILAR and was repeated until the desired number of layers was grown between the materials. Zinc sulfide was grown using a similar procedure as above using 0.2 mM $ZnOAc_2$ in MeOH. Samples which were annealed were heated in a tube furnace under flowing N_2 at 300°C for 20 min

Cation Exchange Reactions: Cation exchange reactions were performed on attached CdSe/CdS samples with 6 monolayers of CdS grown at the interfaces. For conversion to $Cu_{2-x}Se/Cu_{2-x}S$ we used methods similar to those previously reported however we did not precisely control for concentration of metal ions exchanged.[51] Briefly, we dipped our CdSe/CdS assemblies (on a Au TEM grid) in a 2 mg/ml solution of tetrakis(acetonitrile) copper(i) hexaflurophosphate in methanol for 5 min followed by rinsing the film in methanol. For subsequent conversion to HgSe/HgS the previously prepared $Cu_{2-x}Se/Cu_{2-x}S$ films were immersed

in a solution containing 6 mg $Hg(NO_3)_2$ in 3 ml of MeOH with 2μl of tributylphosphine added for 5min and subsequently rinsed with MeOH.

TEM and Electron Diffraction Characterization: TEM, selected area electron diffraction (SAED), and HRTEM was performed on an FEI Tecnai T20 S-TWIN TEM operating at 200 kV with a LaB_6 filament. TEM images and diffraction patterns were collected using a Gatan Rio 16IS camera with full 4k by 4k resolution and images were collected using the drift correction feature, which collects images at 20 fps, calculates the drift between subsequent images, removes the drift, and sums the images. Diffraction patterns are collected in a summing mode (without drift correction) to simultaneously achieve high dynamic range and high signal to noise. Low magnification images were collected with a 30 μm objective aperture and HRTEM images were collected without an objective aperture. HRTEM images were taken near Scherzer focus, which resulted in dark atom contrast for this crystal thickness. Wide angle and small angle SAED patterns were collected using an $\sim 11\mu m^2$ area diffraction aperture with a nominal camera length of 300mm and 4.6m respectively. For small angle-SAED the convergence angle of the illumination was kept constant by using a fixed "spot size" and C2 lens excitation for all samples. For small angle-SAED, the diffraction stigmation was carefully adjusted to ensure a round transmitted beam. The diffraction camera length for small angle-SAED was calibrated using the inter-planar spacing of the native assembled sample determined *via* TEM images. Diffraction rotation for wide angle SAED was measured using a MoO_3 standard and for small angle-SAED was determined by comparing real-space superlattice images with diffraction patterns.

TEM Image Analysis: All images and diffraction patterns were rotated using bilinear interpolation in ImageJ so that the crystal alignment was consistent throughout the figures. For all FTs displayed and analyzed, care was taken to avoid streaking artifacts that result from image edges. Briefly in Gatan Digital Micrograph 3.0 (GMS 3.0), a $2^n \times 2^n$ pixel area of interest was cropped from the image and was subsequently multiplied by a 2D Hanning window followed by computing the FT. For visualization, the log of the modulus of the

FT was saved and visualized in ImageJ using the "fire" lookup table to facilitate viewing. Diffraction patterns were radially and azimuthally integrated using the Difftools package[52] for GMS 3.0. 2D Autocorrelation functions were calculated from raw TEM images or STEM EDS maps using GMS 3.0. For TEM images, the autocorrelation was normalized to the intensity of the first peak in the $\Gamma - M$ ($[11\bar{2}0]_{SL}$) direction to eliminate diffraction contrast modulations damping the autocorrelation envelope.[34] Since STEM-EDS maps provide linear contrast, the autocorrelation was normalized to the height of the central peak avoiding the exact origin (zero pixel shift).[53] 2D autocorrelation images were displayed using the "fire" lookup table ensuring the same minimum and maximum values were used to define the lookup table bounds. Autocorrelation profiles were extracted along the $\Gamma - M$ ($[11\bar{2}0]$) direction using ImageJ.

HRSTEM and STEM-EDS Characterization: High angle annular dark field- HAADF STEM and STEM EDS maps was collected on the FEI TitanX 60-300 microscope at the National Center for Electron Microscopy, Molecular Foundry, Lawrence Berkeley National Laboratory (LBNL). An FEI low background double tilt holder was used for all experiments. HAADF STEM was performed at 300kV with a beam convergence semi-angle of 10 mrad using a Fischione high-angle annular dark-field (HAADF) detector with an inner semiangle, β, of 63 mrad. STEM-EDS mapping was performed at 200kV with a typical probe current of ∼850 pA using an FEI Super-X Quad windowless detector with a solid angle of 0.7 steradians. Data was collected using the Bruker Esprit software utilizing drift correction. High resolution maps were collected with a 2 Å pixel size with a typical collection time of ∼15 min, after which the sample was damaged too much. Data displayed in Figure 3 and Figure S16 are unmodified raw counts while Figure 6 used a 3 pixel average filter. Fourier transforms and autocorrelations used the unmodified maps for all cases. Quantification was performed using the Bruker Esprit software using the Cliff-Lorimer method. The following spectral lines were used for each element: Cd L-series, Se K-series, S K-series, Cu K-series series Hg L-series series. Samples for cation exchange experiments were prepared on Au

TEM grids, while standard CdSe/CdS/Cd(Zn)S samples used Cu TEM grids.

X-ray Diffraction: For ensemble characterization of NC starting materials, solids were made into fine powders to avoid orientation effects. Powders were prepared by depositing a large amount of NCs from hexanes onto a glass slide, and allowed to dry, the film was then scraped off the glass slide with a clean razor blade onto a $\langle 510 \rangle$ oriented Si low background diffraction substrate. For XRD characterization of nanocrystal assemblies, NCs were assembled as described above and scooped onto thin glass coverslips where subsequent attachment reactions were performed. The thin glass coverslip was placed on top of the $\langle 510 \rangle$ oriented Si substrate. Diffraction patterns were collected on a Bruker Phaser D2 diffractometer with Cu $k\alpha$ source operated at 30 kV and 10 mA with a 160 SSD detector. Diffraction patterns were collected from 20° to 60° 2θ with a step size of 0.02°, an integration time of 7s per step. For samples on glass coverslips, the amorphous scattering background was removed using the diffracEVA software. X-ray diffraction and electron diffraction data were plotted in Q ($Q = \frac{2\pi}{d}$) space for easier comparison.

Optical Characterization: Samples for optical characterization were prepared by scooping initial samples onto glass coverslips and performing the desired SILAR or heat treatments. Steady state PL spectra and and TRPL lifetimes were collected using a Picoquant Fluotime 300 spectrometer, a PMA 175 detector, and a LDH-P-C-405 diode laser with a 407 nm excitation wavelength (50 ps pulse width) and typically using a laser repetition rate of 4MHz.

FTIR Spectroscopy: Samples for FTIR spectroscopy were prepared on CaF_2 substrates and subjected to identical surface chemistry treatments used for TEM and optical studies. After each treatment, the substrate was placed in a ∼50°C vacuum oven to remove residual solvents for ∼30 min. FTIR spectra were collected using a Thermo Fischer Nicolet iS10 in transmission geometry. Spectra were blanked to an empty beam-path. Spectra from 3 different areas were collected from each sample to average out sample inhomogeneity.

Computational Methods: To generate the atomic configurations for the electronic

structure calculations, we first prepared faceted CdSe QD ("cores") with a diameter of 1.2 nm. Next, additional monolayers of the desired material (CdSe, CdS, or ZnS) were added layer by layer to achieve the desired sizes of the cores and shell(s). To do this, additional chalcogenide (metal) atoms were bonded to the surface metal (chalcogenide) atoms with the appropriate translations to maintain the wurtzite crystal structure. Next, atoms with fewer than 2 bonds were then removed, completing the addition of a monolayer while preserving faceting. This process was repeated until the desired core/shell structure was generated.

QD dimers and trimers were prepared by starting with two CdSe cores separated by an integer lattice translation of the desired distance. Material (CdSe, CdS or ZnS) was added until the QDs reached the desired size and atomic neck thickness. For the variation of interfacial area and the asymmetrical trimers, the above method for layer by layer growth was applied but restricted to the QD-QD interface while keeping the dot-to-dot distance fixed. For the variation of dot-to-dot distance with a fixed neck thickness, first a QD dimer was generated by the aforementioned procedure resulting in a fused dimer with a given neck thickness. Next the structure was split halfway along the bond axis and additional integer lattice translations were added to the separation. Finally, the resulting void between the QDs was filled by duplicating atoms from the original QD dimer's QD-QD interface, reforming the QD-QD bond. Each structure was manually checked to verify the consistency of the desired structural parameter(s).

These initial structures were then used as inputs for molecular dynamics based structural minimization using Stillinger-Weber interaction potentials[54] using LAAMPS,[55] dangling bond passivation,[38] and the calculation of single particle carrier (*i.e.* electron and hole) states using the semi-empirical pseudopotential method[36] and filter-diagonalization techniques,[35,56] as discussed in detail previously.[24] Atomic models with corresponding carrier densities were rendered using VESTA.[57]

Acknowledgement

Nanocrystal synthesis, assembly, attachment, and structural characterization were supported by the National Science Foundation, Division of Materials Research (DMR), under Award Number DMR-1808151. Theoretical, optical characterization, and cation exchange portions of this work were synergistically supported by the U.S. Department of Energy, Office of Science, Office of Basic Energy Sciences, Materials Sciences and Engineering Division, under Contract No. DE- AC02-05-CH11231, within the Physical Chemistry of Inorganic Nanostructures Program (KC3103). This work made use of the MGCF at UC Berkeley which is supported by NIH S10OD023532. Work at the Molecular Foundry was supported by the Office of Science, Office of Basic Energy Sciences, of the U.S. Department of Energy under Contract No. DE-AC02-05CH11231. J.C.O gratefully acknowledges the support of the Kavli Philomathia Graduate Student Fellowship. The authors like to thank Dr. Chang Yan for help with IR spectroscopy measurements, Dr. Arunima Balan for help with PL and TRPL measurements, Dr. Assaf Ben-Moshe for useful discussions and Dr. Karen Bustillo for support on the TitanX microscope at the National Center for Electron Microscopy.

Supporting Information Available

The Supporting Information is available free of charge on the ACS Publications website at DOI:XXX

Figure S1-Figure S27 (PDF) Additional TEM, STEM, PL, and electron diffraction characterization. Additional details related to theoretical calculations.

Tables S1-S4 (PDF) Additional Structural parameters of superlattice assemblies

References

1. Banin, U.; Cao, Y.; Katz, D.; Millo, O. Identification of Atomic-Like Electronic States in Indium Arsenide Nanocrystal Quantum Dots. *Nature* **1999**, *400*, 542–544.

2. Alivisatos, A. P. Semiconductor Clusters, Nanocrystals, and Quantum Dots. *Science* **1996**, *271*, 933–937.

3. Murray, C. B.; Kagan, C. R.; Bawendi, M. G. Self-Organization of CdSe Nanocrystallites into Three-Dimensional Quantum Dot Superlattices. *Science* **1995**, *270*, 1335–1338.

4. Shevchenko, E. V.; Talapin, D. V.; Murray, C. B.; O'Brien, S. Structural Characterization of Self-Assembled Multifunctional Binary Nanoparticle Superlattices. *Journal of the American Chemical Society* **2006**, *128*, 3620–3637.

5. Yang, J.; Wise, F. W. Effects of Disorder on Electronic Properties of Nanocrystal Assemblies. *Journal of Physical Chemistry C* **2015**, *119*, 3338–3347.

6. Luther, J. M.; Law, M.; Song, Q.; Perkins, C. L.; Beard, M. C.; Nozik, A. J. Structural, Optical, and Electrical Properties of Self-Assembled Films of PbSe Nanocrystals Treated with 1,2-Ethanedithiol. *ACS nano* **2008**, *2*, 271–80.

7. Yazdani, N.; Andermatt, S.; Yarema, M.; Farto, V.; Bani-Hashemian, M. H.; Volk, S.; Lin, W. M. M.; Yarema, O.; Luisier, M.; Wood, V. Charge Transport in Semiconductors Assembled from Nanocrystal Quantum Dots. *Nature Communications* **2020**, *11*, 2852.

8. Law, M.; Luther, J. M.; Song, Q.; Hughes, B. K.; Perkins, C. L.; Nozik, A. J. Structural, Optical, and Electrical Properties of PbSe Nanocrystal Solids Treated Thermally or with Simple Amines. *Journal of the American Chemical Society* **2008**, *130*, 5974–85.

9. Kovalenko, M. V.; Scheele, M.; Talapin, D. V. Colloidal Nanocrystals with Molecular Metal Chalcogenide Surface Ligands. *Science* **2009**, *324*, 1417–20.

10. Gilmore, R. H.; Winslow, S. W.; Lee, E. M.; Ashner, M. N.; Yager, K. G.; Willard, A. P.; Tisdale, W. A. Inverse Temperature Dependence of Charge Carrier Hopping in Quantum Dot Solids. *ACS Nano* **2018**, *12*, 7741–7749.

11. Gilmore, R. H.; Lee, E. M.; Weidman, M. C.; Willard, A. P.; Tisdale, W. A. Charge Carrier Hopping Dynamics in Homogeneously Broadened PbS Quantum Dot Solids. *Nano Letters* **2017**, *17*, 893–901.

12. Kang, M. S.; Sahu, A.; Norris, D. J.; Frisbie, C. D. Size-Dependent Electrical Transport in CdSe Nanocrystal Thin Films. *Nano Letters* **2010**, *10*, 3727–3732.

13. Baumgardner, W. J.; Whitham, K.; Hanrath, T. Confined-But-Connected Quantum Solids *via* Controlled Ligand Displacement. *Nano Letters* **2013**, *13*, 3225–3231.

14. Boneschanscher, M.; Evers, W. H.; Geuchies, J. J.; Altlantzis, T.; Goris, B.; Rabouw, F.; van Rossum, S. A. P.; van der Zant, H. S. J.; Siebbeles, L. D. A.; Van Tendeloo, G.; Swart, I.; Hilhorst, J.; Petukhov, A.; Bals, S.; Vanmaekelbergh, D. Long-Range Orientation and Atomic Attachment of Nanocrystals in 2D Honeycomb Superlattices. *Science* **2014**, *344*, 1377–1380.

15. Whitham, K.; Yang, J.; Savitzky, B. H.; Kourkoutis, L. F.; Wise, F.; Hanrath, T. Charge Transport and Localization in Atomically Coherent Quantum Dot Solids. *Nature Materials* **2016**, *15*, 557–563.

16. van Overbeek, C.; Peters, J. L.; van Rossum, S. A. P.; Smits, M.; van Huis, M. A.; Vanmaekelbergh, D. Interfacial Self-Assembly and Oriented Attachment in the Family of PbX (X = S, Se, Te) Nanocrystals. *The Journal of Physical Chemistry C* **2018**, *122*, 12464–12473.

17. Evers, W. H.; Schins, J. M.; Aerts, M.; Kulkarni, A.; Capiod, P.; Berthe, M.; Grandidier, B.; Delerue, C.; Zant, H. S. J. V. D.; Overbeek, C. V.; Peters, J. L.; Vanmaekelbergh, D.; Siebbeles, L. D. a. High Charge Mobility in Two-Dimensional Percolative

Networks of PbSe Quantum Dots Connected by Atomic Bonds. *Nature Communications* **2015**, *6*, 1–8.

18. Kalesaki, E.; Evers, W. H.; Allan, G.; Vanmaekelbergh, D.; Delerue, C. Electronic Structure of Atomically Coherent Square Semiconductor Superlattices with Dimensionality Below Two. *Physical Review B - Condensed Matter and Materials Physics* **2013**, *88*, 1–9.

19. Anderson, P. W. Absence of Diffusion in Certain Random Lattices. *Physical Review* **1958**, *109*, 1492–1505.

20. Savitzky, B. H.; Hovden, R.; Whitham, K.; Yang, J.; Wise, F.; Hanrath, T.; Kourkoutis, L. F. Propagation of Structural Disorder in Epitaxially Connected Quantum Dot Solids from Atomic to Micron Scale. *Nano Letters* **2016**, *16*, 5714–5718.

21. Reich, K. V.; Shklovskii, B. I. Exciton Transfer in Array of Epitaxially Connected Nanocrystals. *ACS Nano* **2016**, *10*, 10267–10274.

22. Treml, B. E.; Savitzky, B. H.; Tirmzi, A. M.; Dasilva, J. C.; Kourkoutis, L. F.; Hanrath, T. Successive Ionic Layer Absorption and Reaction for Postassembly Control over Inorganic Interdot Bonds in Long-Range Ordered Nanocrystal Films. *ACS Applied Materials and Interfaces* **2017**, *9*, 13500–13507.

23. Walravens, W.; Solano, E.; Geenen, F.; Dendooven, J.; Gorobtsov, O.; Tadjine, A.; Mahmoud, N.; Ding, P. P.; Ruff, J. P.; Singer, A.; Roelkens, G.; Delerue, C.; Detavernier, C.; Hens, Z. Setting Carriers Free: Healing Faulty Interfaces Promotes Delocalization and Transport in Nanocrystal Solids. *ACS Nano* **2019**, *13*, 12774–12786.

24. Ondry, J. C.; Philbin, J. P.; Lostica, M.; Rabani, E.; Alivisatos, A. P. Resilient Pathways to Atomic Attachment of Quantum Dot Dimers and Artificial Solids from Faceted CdSe Quantum Dot Building Blocks. *ACS Nano* **2019**, *13*, 12322–12344.

25. Wang, Y.; Pu, C.; Lei, H.; Qin, H.; Peng, X. CdSe@CdS Dot@Platelet Nanocrystals: Controlled Epitaxy, Monoexponential Decay of Two-Dimensional Exciton, and Non-Blinking Photoluminescence of Single Nanocrystal. *Journal of the American Chemical Society* **2019**, *141*, 17617–17628.

26. Cassette, E.; Mahler, B.; Guigner, J. M.; Patriarche, G.; Dubertret, B.; Pons, T. Colloidal CdSe/CdS Dot-in-Plate Nanocrystals with 2D-Polarized Emission. *ACS Nano* **2012**, *6*, 6741–6750.

27. Dong, A.; Chen, J.; Vora, P. M.; Kikkawa, J. M.; Murray, C. B. Binary Nanocrystal Superlattice Membranes Self-Assembled at the Liquid-Air Interface. *Nature* **2010**, *466*, 474–477.

28. Webber, D. H.; Brutchey, R. L. Ligand Exchange on Colloidal CdSe Nanocrystals Using Thermally Labile *tert*-Butylthiol for Improved Photocurrent in Nanocrystal Films. *Journal of the American Chemical Society* **2012**, *134*, 1085–1092.

29. Pathan, H. M.; Lokhande, C. D. Deposition of Metal Chalcogenide Thin Films by Successive Ionic Layer Adsorption and Reaction (SILAR) Method. *Bull. Mater. Sci.* **2004**, *27*, 85–111.

30. Van Der Stam, W.; Gantapara, A. P.; Akkerman, Q. A.; Soligno, G.; Meeldijk, J. D.; Van Roij, R.; Dijkstra, M.; De Mello Donega, C. Self-Assembly of Colloidal Hexagonal Bipyramid- and Bifrustum-Shaped ZnS Nanocrystals into Two-Dimensional Superstructures. *Nano Letters* **2014**, *14*, 1032–1037.

31. Van Der Stam, W.; Rabouw, F. T.; Vonk, S. J.; Geuchies, J. J.; Ligthart, H.; Petukhov, A. V.; De Mello Donega, C. Oleic Acid-Induced Atomic Alignment of ZnS Polyhedral Nanocrystals. *Nano Letters* **2016**, *16*, 2608–2614.

32. Dong, A.; Jiao, Y.; Milliron, D. J. Electronically Coupled Nanocrystal Superlattice Films by *in Situ* Ligand Exchange at the Liquid-Air Interface. *ACS nano* **2013**, *7*, 10978–84.

33. Abelson, A.; Qian, C.; Salk, T.; Luan, Z.; Fu, K.; Zheng, J.-G.; Wardini, J. L.; Law, M. Collective Topo-Epitaxy in the Self-Assembly of a 3D Quantum Dot Superlattice. *Nature Materials* **2020**, *19*, 49–55.

34. Pichler, S.; Bodnarchuk, M. I.; Kovalenko, M. V.; Yarema, M.; Springholz, G.; Talapin, D. V.; Heiss, W. Evaluation of Ordering in Single-Component and Binary Nanocrystal Superlattices by Analysis of Their Autocorrelation Functions. *ACS Nano* **2011**, *5*, 1703–1712.

35. Toledo, S.; Rabani, E. Very Large Electronic Structure Calculations using an Out-of-Core Filter-Diagonalization Method. *Journal of Computational Physics* **2002**, *180*, 256–269.

36. Wang, L. W.; Zunger, A. Local-Density-Derived Semiempirical Pseudopotentials. *Physical Review B* **1995**, *51*, 17398–17416.

37. Balan, A. D.; Eshet, H.; Olshansky, J. H.; Lee, Y. V.; Rabani, E.; Alivisatos, A. P. Effect of Thermal Fluctuations on the Radiative Rate in Core/Shell Quantum Dots. *Nano Letters* **2017**, *17*, 1629–1636.

38. Eshet, H.; Grünwald, M.; Rabani, E. The Electronic Structure of CdSe/CdS Core/Shell Seeded Nanorods: Type-I or Quasi-Type-II? *Nano Letters* **2013**, *13*, 5880–5885.

39. De Trizio, L.; Manna, L. Forging Colloidal Nanostructures *via* Cation Exchange Reactions. *Chemical Reviews* **2016**, *116*, 10852–10887.

40. Lan, X.; Chen, M.; Hudson, M. H.; Kamysbayev, V.; Wang, Y.; Guyot-Sionnest, P.; Talapin, D. V. Quantum Dot Solids Showing State-Resolved Band-Like Transport. *Nature Materials* **2020**,

41. Li, H.; Zanella, M.; Genovese, A.; Povia, M.; Falqui, A.; Giannini, C.; Manna, L. Sequential Cation Exchange in Nanocrystals: Preservation of Crystal Phase and Formation of Metastable Phases. *Nano letters* **2011**, *11*, 4964–70.

42. Tu, R.; Xie, Y.; Bertoni, G.; Lak, A.; Gaspari, R.; Rapallo, A.; Cavalli, A.; Trizio, L. D.; Manna, L. Influence of the Ion Coordination Number on Cation Exchange Reactions with Copper Telluride Nanocrystals. *Journal of the American Chemical Society* **2016**, *138*, 7082–7090.

43. DaSilva, J. C.; Smeaton, M. A.; Dunbar, T. A.; Xu, Y.; Balazs, D. M.; Kourkoutis, L. F.; Hanrath, T. Mechanistic Insights into Superlattice Transformation at a Single Nanocrystal Level Using Nanobeam Electron Diffraction. *Nano Letters* **2020**, *20*, 5267–5274.

44. McCray, A. R. C.; Savitzky, B. H.; Whitham, K.; Hanrath, T.; Kourkoutis, L. F. Orientational Disorder in Epitaxially Connected Quantum Dot Solids. *ACS Nano* **2019**, *13*, 11460–11468.

45. Peters, J. L.; Altantzis, T.; Lobato, I.; Jazi, M. A.; van Overbeek, C.; Bals, S.; Vanmaekelbergh, D.; Sinai, S. B. Mono- and Multilayer Silicene-Type Honeycomb Lattices by Oriented Attachment of PbSe Nanocrystals: Synthesis, Structural Characterization, and Analysis of the Disorder. *Chemistry of Materials* **2018**, *30*, 4831–4837.

46. Scheibner, M.; Schmidt, T.; Worschech, L.; Forchel, A.; Bacher, G.; Passow, T.; Hommel, D. Superradiance of Quantum Dots. *Nature Physics* **2007**, *3*, 106–110.

47. Rainò, G.; Becker, M. A.; Bodnarchuk, M. I.; Mahrt, R. F.; Kovalenko, M. V.; Stöferle, T. Superfluorescence from Lead Halide Perovskite Quantum Dot Superlattices. *Nature* **2018**, *563*, 671–675.

48. Carbone, L.; Nobile, C.; De Giorgi, M.; Sala, F. D.; Morello, G.; Pompa, P.; Hytch, M.; Snoeck, E.; Fiore, A.; Franchini, I. R.; Nadasan, M.; Silvestre, A. F.; Chiodo, L.; Kudera, S.; Cingolani, R.; Krahne, R.; Manna, L. Synthesis and Micrometer-Scale Assembly of Colloidal CdSe/CdS Nanorods Prepared by a Seeded Growth Approach. *Nano letters* **2007**, *7*, 2942–50.

49. Jasieniak, J.; Smith, L.; Embden, J. V.; Mulvaney, P. Re-Examination of the Size-Dependent Absorption Properties of CdSe Quantum Dots. **2009**, 19468–19474.

50. Chen, O.; Zhao, J.; Chauhan, V. P.; Cui, J.; Wong, C.; Harris, D. K.; Wei, H.; Han, H.-S.; Fukumura, D.; Jain, R. K.; Bawendi, M. G. Compact High-Quality CdSe–CdS Core–Shell Nanocrystals with Narrow Emission Linewidths and Suppressed Blinking. *Nature Materials* **2013**, *12*, 445–451.

51. Rivest, J. B.; Buonsanti, R.; Pick, T. E.; Zhu, L.; Lim, E.; Clavero, C.; Schaible, E.; Helms, B. A.; Milliron, D. J. Evolution of Ordered Metal Chalcogenide Architectures Through Chemical Transformations. *Journal of the American Chemical Society* **2013**, *135*, 7446–9.

52. Mitchell, D. R. G. DiffTools: Electron Diffraction Software Tools for Digital Micrograph. *Microscopy Research and Technique* **2008**, *71*, 588–593.

53. Robertson, C. Theory and Practical Recommendations for Autocorrelation-Based Image Correlation Spectroscopy. *Journal of Biomedical Optics* **2012**, *17*, 080801.

54. Zhou, X. W.; Ward, D. K.; Martin, J. E.; Van Swol, F. B.; Cruz-Campa, J. L.; Zubia, D. Stillinger-Weber Potential for the II-VI Elements Zn-Cd-Hg-S-Se-Te. *Physical Review B - Condensed Matter and Materials Physics* **2013**, *88*, 1–14.

55. Plimpton, S. Fast Parallel Algorithms for Short-Range Molecular Dynamics. *Journal of Computational Physics* **1995**, *117*, 1–19.

56. Wall, M. R.; Neuhauser, D. Extraction, Through Filter-Diagonalization, of General Quantum Eigenvalues or Classical Normal Mode Frequencies from a Small Number of Residues or a Short-Time Segment of a Signal. I. Theory and Application to a Quantum-Dynamics Model. *The Journal of Chemical Physics* **1995**, *102*, 8011–8022.

57. Momma, K.; Izumi, F. VESTA 3 for Three-Dimensional Visualization of Crystal, Volumetric and Morphology Data. *Journal of Applied Crystallography* **2011**, *44*, 1272–1276.

Graphical TOC Entry